Punjab University Journal of Mathematics (2025), 57(04), 374-403
https://doi.org/10.52280/pujm.2025.57(04)02

Neural Computing Approach to the Flow and Thermal Analysis of Ternary Hybrid Nanofluid Over Wedges

Saraj Khan
Department of Mathematics, University of Management and Technology, Lahore, Pakistan

*Muhammad Imran Asjad
Department of Mathematics, University of Management and Technology, Lahore, Pakistan

Abdul Wahab
Department of Mathematics, University of Management and Technology, Lahore, Pakistan

*Corresponding Author
imran.asjad@umt.edu.pk

Received
25 February, 2025

Accepted
17 October, 2025

Published Online
13 November, 2025

Abstract. The steady state motion of a ternary hybrid nanofluid across a permeable wedge is investigated in the case when the wedge is stretching or contracting. An applied magnetic field and the effect of radiation are included in the analysis. An application of a similarity transformation to the governing equations that describe the flow of ternary hybrid nanofluid results in the conversion of those equations into ordinary differential equations. All of these equations are solved numerically using the bvp4c solver in MATLAB. Additionally, the flow of the ternary hybrid nanofluid is governed by the nonlinear differential equations that are then solved by a hybrid approach combining artificial neural networks with Levenberg–Marquardt backpropagation technique. The performance and hence the comparison of algorithms are carried out using regression analysis, error histograms, function fitting graphs, and mean squared error results. To achieve the desired results, the considered parameters are varied systematically to be the stretching/shrinking parameter (λ), the magnetic parameter (M), the suction/injection parameter (S), the wedge angle (m), and the radiation parameter (Rd). In terms of performance, the velocity and temperature profiles for the proposed model demonstrated strong accuracy, as evidenced by the mean squared error values of $[2.251 \times 10^{-9},\ 5.5339 \times 10^{-10},\ 1.2449 \times 10^{-9},\ 1.7511 \times 10^{-8},\ 3.1377 \times 10^{-9}]$. According to the investigation, solutions are found up to a particular suction and stretching/shrinking strength. An increase in the wedge angle parameter, the critical value associated with the thermal response decreases. Additionally, the heat transfer rate provided by the ternary hybrid nanofluid is greater than those possessed by the conventional nanofluids. Moreover, an increase in the radiation parameter enhances the heat transferring rate.

AMS (MOS) Subject Classification Codes: 35Q51; 35C07; 25U09; 35Q53
Key Words: Ternary hybrid nanofluid, Magnetic field, Stretching/shrinking wedge, Artificial neural networks, Similarity transformation.

1. INTRODUCTION

Neural networks and computational intelligence are used to examine the distinctive characteristics of ternary hybrid nanofluid systems. Artificial neural networks (ANNs) are mimics of those in human brain in structure and function (like biological neurons) [25, 11]. An ANN is a multi-layer system that includes input layers, one or more hidden layers, and an output layer. Sigmoid function are activation functions which processes the incoming signals in each neuron and pass it out as output signals to the next layer. Neurons have connections to other neurons, and connections have weights, which are measures of the strength of this connection. In this, some weights are modified throughout learning via input information and wanted yields. In natural language processing, image processing, pattern identification, machine learning, and artificial intelligence (AI) [25, 1], ANNs are in use. Powerful tools, they are for solving complex problems and have made great advances in science and technology. In the past few years, the adoptions of advanced technology have boomed across industries with the need for efficient heat transfer, namely power generation, automotive systems, and electronics. As these fields grow, there is a demand for smaller devices with better storage and performance, creating opportunities for breakthroughs in cooling technology. The first guides that produced a marked increase in the thermal performance of base fluids, composed of kerosene, water, motor oil, or ethylene glycol, with high heat conductivity and micrometer-sized particles, are those of Maxwell.

Ternary hybrid nanofluids are considered an advanced category of engineered fluids, consisting of three different nanoparticles dispersed in a common base fluid. Numerical investigation of the magnetohydrodynamic (MHD) impact on Maxwell nanofluids has been carried out in recent studies, highlighting their non-Newtonian behavior and heat transfer characteristics [53, 19]. These works provide a useful benchmark for extending advanced modeling approaches to complex fluid systems. The concept of a standard nanofluid, which involves a single type of nanoparticle, was first introduced by Choi and Eastman [9]. Several researchers have performed numerical analyses on heat transfer and boundary layer flow involving hybrid nanofluids. The movement of a mixed nanofluid containing $Cu-Al_2O_3$ nanoparticles along a stretched surface that exhibits magnetic phenomena was examined by Devi and S. S. U Devi [10]. After beginning their investigation, they extended it to three-dimensional flow under Newtonian warming conditions. In both instances, the novel nanofluid outperformed conventional nanofluids in terms of thermal transfer rate. Hayat and Nadeem examined the rotational flow of a hybrid nanofluid $Ag-CuO/$water [14]. A related issue is also examined in the research of Hayat et al. [15]. Alam et al. [4] examine unsteady induced convection boundary-layer motion across a porous expanding/contracting wedge having fluctuating Schmidt and Prandtl numbers in a setting of varying fluid properties and thermal analysis.

Recent studies have expanded the scope of ternary hybrid nanofluid research by examining the combined effects of magnetic fields, slip conditions, and surface-catalyzed reactions on complex flow systems. For instance, investigations on rotating flows under inclined magnetic fields have highlighted the role of irreversibility in transport phenomena [35]. Similarly, oscillating magnetic fields applied to flows between spinning disks were analyzed within the framework of Thompson and Troian slip and a modified Fourier's law, providing new insights into energy transport [36]. Additional contributions have addressed stretching surface flows influenced by induced magnetic fields and catalytic reactions [37], while other works have explored ferromagnetic ternary and hybrid nanofluid flows, emphasizing entropy generation and reaction effects [44]. Together, these studies underscore the growing importance of magnetic and catalytic interactions in shaping the thermal and flow behavior of advanced nanofluids.

There is widespread concern about energy shortages in many places. This problem requires new models. Solar power is one solution, and it becomes more and more important. Sunlight can be converted into usable energy for use in industries as well as homes. Among the many uses of thermal radiation, a type of solar energy, are heating and cooling of spaces, heating large water reservoirs, and industrial and environmental applications. Further information on studies of thermal radiative heat transfer is found in references [40, 16]. Awaludin et al. [6] examined the stability of MHD flow within the boundary layer over a stretching or shrinking wedge. A numerical analysis is conducted to investigate heat transfer and the steady two-dimensional MHD boundary layer flow along a porous wedge that undergoes stretching or shrinking. They find the potential of several solutions to be in the area of falling strength. They conducted a stability study to ascertain the most stable and physically dependable option. A viscous, incompressible fluid's forced convective laminar flow across a spinning disk has been examined in relation to thermophoresis effects by Rahman and Postelnicu [34]. Postelnicu also explored the influence of heat transfer on particle formation during convection over inclined surfaces within a permeable medium [33]. Shehzad et al. [45] analyzed how thermophoresis influences mixed convection flow under diverse temperature and flow conditions. Khan et al. [24] investigated the MHD flow for a nanofluid across a nonlinearly extending or decreasing wedge incorporating nonlinear radiative impacts. The thermal analysis and Brownian motion effects are accounted for in the framework of passively analyzing nanofluids, but the steady flow of a nanofluid over a moving wedge and the MHD effects are studied. The thermal energy equation incorporates nonlinear radiative effects.

Su and his team researched MHD mixed convective heat transfer over a porous stretching wedge, taking into account thermal radiation and ohmic heating effects [47]. An investigation of the MHD mixed convective flow and heat transfer of an incompressible, dense, electrically conductive fluid over a stretched porous wedge with the consideration of radiant heat and ohmic heating is conducted. For this analysis, a novel analytical approach referred to as the DTM-BF method was utilized. Nadeem et al. [31] carried out a computational analysis of the Falkner-Skan wedge problem for a stationary as well as a moving wedge. A viscous fluid flowing along the highest point of a stationary or movable wedge was examined in relation to the properties of the produced magnetic field. In addition, they calculated heat flux employing Fourier's law for heat conduction. Kumari et al. [26, 8, 17]

explored the behavior of magnetic fluids and heat transfer phenomena over a stretching surface. They also recognized three types of minute particles, namely Cu, Al_2O_3, and TiO_2, which are distributed within water as the base fluid. Therefore, Ghosh et al. [21, 49, 13] analyzed unsteady fluid flow near a stagnation point, where the fluid motion becomes stationary, under the influence of a magnetic field. Ali et al. [5] investigated how heat moves and how fluid flows near a surface that is stretching and under the influence of a magnetic field. A study by Nadeem and Akram [30] examined the flow of a certain kind of fluid in an irregular channel with respect to a magnetic field. Mekheimer [29] studied the way a specific kind of fluid behaves, where it moves in wave-like shapes yet is affected by a magnetized field.

Advanced thermal regulation using ferromagnetic hybrid nanoparticles was studied by Khan et al. [22, 23] through Levenberg–Marquardt neural networks. Zainal et al. [54] investigated MHD heat transfer over a moving wedge, focusing on edge conditions for flow and thermal behavior. The role of viscous dissipation, heat generation, and absorption on fluid flow has also been examined. Sulochana et al. [48] analyzed MHD Casson fluid flow over a wedge, showing how chemical reactions and thermal radiation influence heat and mass transfer. Rana et al. [38] performed numerical and sensitivity studies on nanoliquid flow and heat transfer over a wedge using a modified Buongiorno model. Siddique et al. [46] explored second-grade fuzzy mixed nanofluid flow over a wedge-like Riga surface, highlighting velocity and temperature effects. Rana et al. [39] further studied $CuO - H_2O$ nanoliquid over a wedge, accounting for slip and joule heating. Endalew and Sarkar [12] examined forced convection hyperbolic tangent nanofluid over a porous wedge, considering melting heat transfer. Shah et al. [43] studied magnetized cross nanofluid flow with chemical modeling. Mahanthesh et al. [28] applied response surface optimization to assess $ZnO - EG$ nanoliquid Falkner–Skan wedge flow. Li et al. [27] evaluated heat transfer in rotating wedge-shaped channels with fin structures. Neural network approaches were also used to predict thermal conductivity of nanofluid systems [2, 51].

Jan et al. [20] investigated the impact of magnetic fields and thermal radiation, along with surface geometry, on the flow and heat transfer behavior of ternary hybrid nanofluids. Since the governing equations of such systems are highly nonlinear, accurate and efficient solutions require the use of sophisticated computational techniques. ANNs are becoming very effective means of continuum modelling of nonlinear problems, such as in fluid dynamics and heat transfer. ANNs learn patterns and approximate solutions so, hence and an effective and fruitful alternative is ANNs from traditional numerical methods. However, studies of integration of ANNs with optimization technique like Levenberg Marquardt backpropagation algorithm, show the rapid convergence and accurate prediction behavior for complex flow problems by Sakkaravarthi et al. [42] . An ANN allows for the simultaneous study of many parameters, provides increased understanding of physical phenomena, and decreases computation time in the field of ternary hybrid nanofluid flow and heat transfer analysis. In particular, this hybrid method is very useful to obtain solutions of ternary hybrid nanofluid species over stretching surfaces as well as shrinking surfaces under various physical constraints.

This study aims at filling the present gap by associating the outstanding thermal and flow properties of ternary hybrid nanofluids with an exhaustive investigation of their heat transfer attributes over a stretching or shrinking wedge. The LMBA-ANN approach is used

together with the heat transfer and flow model to take advantage of the potentials of these fluids for enhanced thermal management in the advanced technologies.

The novelty of this study lies in its threefold contribution. First, a hybrid computational methodology combining MATLAB's `bvp4c` solver with Artificial Neural Networks optimized using the Levenberg–Marquardt Backpropagation Algorithm (LMBA) is developed, offering improved convergence and predictive capability compared to traditional approaches. Second, the formulation of a SiO_2–TiO_2–Al_2O_3/H_2O ternary hybrid nanofluid provides enhanced thermal and flow properties beyond those of simple or binary nanofluids. Third, new physical insights into wedge flows are presented by systematically analyzing the effects of wedge angle, magnetic field, suction/injection, and radiation on velocity and temperature distributions. Together, these aspects establish the originality and significance of the present work. Table 1 highlights that earlier studies concentrated on conventional numerical solvers, binary nanofluids, and simplified flow domains, which left important gaps in methodology, material formulation, and physical interpretation. The present research overcomes these limitations by employing a hybrid LMBA–ANN approach, analyzing ternary nanofluids, and providing new insights into wedge flow behavior.

TABLE 1. Gap analysis highlighting the novelty of the present study.

Aspect	**Limitations in Previous Studies**	**Present Contribution (Novelty)**
Methodology	Most works rely only on numerical solvers without integration with data-driven models.	Hybrid LMBA–ANN with bvp4c improves accuracy, convergence, and predictive capability.
Material Formulation	Studies are mainly on simple or binary nanofluids.	Introduction of ternary nanofluid (SiO_2–TiO_2–Al_2O_3/H_2O) with superior thermal features.
Flow Physics	Limited studies on wedge flows, with less focus on effects of suction/injection, radiation, and magnetic fields.	New insights into wedge flows by analyzing wedge angle, suction/injection, magnetic field, and radiation impacts.

The structure of the paper is outlined as follows: The section 1 contains in detail a literature review and introduction, whereas section 2 explains the detailed mathematical formulation of the proposed model. The section 3 is fully devoted to studying the use of the Levenberg-Marquardt method for modeling. In Section 4, the results and a detailed examination of the suggested model are presented. The work is concluded in Section 5, and some avenues for further study are proposed.

2. MATHEMATICAL FORMULATION

Figure 1 illustrates the heat transfer and steady ternary hybrid nanofluid flow along a permeable stretching or shrinking wedge. In this case, x and y are Cartesian coordinates, where y is perpendicular to the wedge and x corresponds to measurements along its surface. The motion of the wedge, whether stretching or shrinking, is governed by the velocity function:

$$u_w(x) = U_w x^m$$

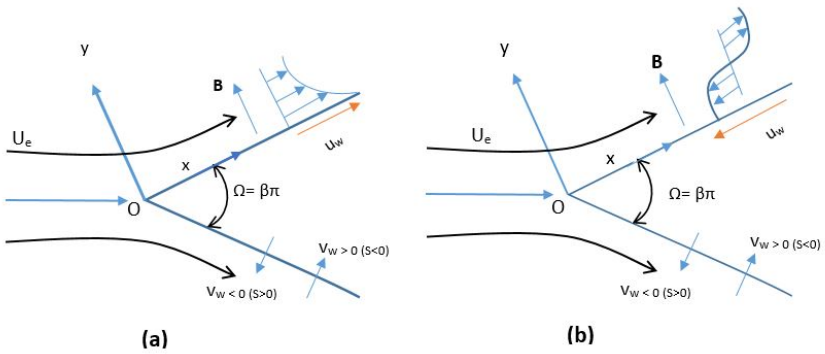

FIGURE 1. Illustration of the coordinate system and physical model: (a) a stretching wedge and (b) a shrinking wedge.

Similarly, the free stream velocity is expressed as:

$$u_e(x) = U_e x^m$$

where $U_e > 0$ is a constant, and U_w determines the type of wedge movement. Specifically, a positive U_w ($U_w > 0$) corresponds to a stretching wedge, a negative U_w ($U_w < 0$) represents a shrinking wedge, and $U_w = 0$ indicates a stationary wedge. The parameter m is defined as:

$$m = \frac{\beta}{2 - \beta}$$

where β and m correspond to the wedge angle and the Hartree pressure gradient parameter, respectively. The total wedge angle is given by:

$$\Omega = \beta\Pi.$$

The parameter m varies within the range $0 \leq m \leq 1$. When the stagnation point flow is directed toward a vertical flat surface ($\Omega = \Pi$), the corresponding value is $m = 1$ ($\beta = 1$). Conversely, for flow over a horizontal flat surface ($\Omega = 0$), the value is $m = 0$ ($\beta = 0$). Furthermore, the acute angle of the wedge is characterized by m and is constrained within the range $0.1 \leq m \leq 0.3$, while the wedge angle Ω lies between 0 and $\Pi/2$. The ambient temperature of the ternary hybrid nanofluid is represented by T_∞, whereas the wedge, whether stretching or shrinking, maintains a constant temperature T_w.
The externally applied magnetic field $B(x)$ along the y-direction is defined as:

$$B(x) = B_\circ x^{(m-1)/2}$$

where $B_\circ$ denotes the strength of the applied magnetic field. The induced magnetic field is disregarded by assuming a negligible magnetic Reynolds number.

The governing equations of the ternary hybrid nanofluid can be expressed in vector form as follows,

$$\nabla \cdot \mathbf{V} = 0, \tag{2. 1}$$

$$\rho_{thnf}\left(\mathbf{V}\cdot\nabla\mathbf{V}\right)=\mu_{thnf}\nabla^2\mathbf{V}-\sigma_{thnf}B^2\left(\mathbf{V}-\mathbf{V}_e\right), \tag{2. 2}$$

$$(\rho C_p)_{thnf}\left(\mathbf{V}\cdot\nabla T\right)=k_{thnf}\nabla^2 T-\nabla\cdot\mathbf{q_r}. \tag{2. 3}$$

In these equations, $\mathbf{V}=(u,v)$ represents the velocity vector of the fluid, while $\mathbf{V}_e=(u_e,0)$ denotes the external velocity.

The associated boundary conditions are expressed as,

$$\begin{cases}\mathbf{V}|_{y=0}=(u_w(x),v_w(x)), & T|_{y=0}=T_w,\\ \mathbf{V}|_{y\to\infty}\to(u_e(x),0), & T|_{y\to\infty}\to T_\infty.\end{cases} \tag{2. 4}$$

A clearer representation of the flow and thermal transport is obtained by rewriting the governing equations of the ternary hybrid nanofluid from their compact vector form into the expanded PDE form as follows [50],

$$\frac{\partial u}{\partial x}+\frac{\partial v}{\partial y}=0, \tag{2. 5}$$

$$\rho_{thnf}\left(u\frac{\partial u}{\partial x}+v\frac{\partial u}{\partial y}\right)=\rho_{thnf}u_e\frac{du_e}{dx}+\mu_{thnf}\frac{\partial^2 u}{\partial y^2}-\sigma_{thnf}B^2(u-u_e), \tag{2. 6}$$

$$k_{thnf}\frac{\partial^2 T}{\partial y^2}=(\rho Cp)_{thnf}\left(u\frac{\partial T}{\partial x}+v\frac{\partial T}{\partial y}\right)+\frac{\partial q_r}{\partial y}, \tag{2. 7}$$

$$\begin{cases}u|_{y=0}=u_w(x), & v|_{y=0}=v_w(x), & T|_{y=0}=T_w,\\ u|_{y\to\infty}\to u_e(x), & v|_{y\to\infty}\to 0, & T|_{y\to\infty}\to T_\infty.\end{cases} \tag{2. 8}$$

For the ternary hybrid nanofluid, u and v indicate the velocity components in the x- and y-direction, respectively. T represents the temperature for the nanofluid, and q_r represents the radiative heat flow. In addition, $v_w(x)$ provides the wall mass transfer velocity.

Based on the Rosseland approximation [41], the radiative heat flux is formulated as [7]:

$$q_r=-\frac{4\sigma_\circ}{3k^*}\times\frac{\partial T^4}{\partial y}, \tag{2. 9}$$

where the Stefan-Boltzmann constant is represented by $\sigma_\circ$ and the mean absorption coefficient by k^*. When we use a Taylor series to expand T^4 about T_∞ while ignoring higher-order components, we get

$$T^4\approx 4T_\infty^3T-3T_\infty^4.$$

Substituting this into the energy equation 2. 7 can be rewritten as

$$u\frac{\partial T}{\partial x}+v\frac{\partial T}{\partial y}=\left(\frac{k_{thnf}}{(\rho Cp)_{thnf}}+\frac{16\sigma_\circ T_\infty^3}{3k^*(\rho Cp)_{thnf}}\right)\frac{\partial^2 T}{\partial y^2}. \tag{2. 10}$$

Furthermore, the following are the parameters and their representations: σ_{thnf} = the ternary hybrid nanofluid's electrical conductivity, k_{thnf} = thermal conductivity, μ_{thnf} = dynamic viscosity, $(\rho Cp)_{thnf}$ = heat capacity, and ρ_{thnf} = density, respectively.

To simplify the governing equations, the following similarity transformation is introduced [52]:

$$\psi = (U_e\nu_f)^{1/2}x^{(m+1)/2}f(\eta),\ \ \theta(\eta) = \frac{T-T_\infty}{T_w-T_\infty},\ \ \eta = \Big(\frac{U_e}{\nu_f}\Big)^{1/2}x^{(m-1)/2}y, \quad (2.\ 11)$$

where ψ is the stream function defined by $u = \frac{\partial\psi}{\partial y}$ and $v = -\frac{\partial\psi}{\partial x}$ which satisfies equation 2. 5 , and ν_f represents the base fluid's kinematic viscosity. Consequently, the velocity components take the form

$$u = U_e x^m f^{'}(\eta),\ \ v = -\frac{m+1}{2}\big(U_e\nu_f\big)^{1/2}x^{(m-1)/2}\bigg(f(\eta) + \frac{m-1}{m+1}\eta f^{'}(\eta)\bigg). \quad (2.\ 12)$$

To ensure similarity, the wall mass transfer velocity is chosen as

$$v_w(x) = -\frac{m+1}{2}\big(U_e\nu_f\big)^{1/2}x^{(m-1)/2}S. \quad (2.\ 13)$$

Here, $S = f(0)$ denotes the constant mass flux parameter. A positive S ($S > 0$) corresponds to fluid suction, while a negative S ($S < 0$) indicates fluid injection or removal. By substituting Equations 2. 11 and 2. 12 into equations 2. 6 and 2. 10 , the transformed governing equations are obtained as

$$\frac{\mu_{thnf}/\mu_f}{\rho_{thnf}/\rho_f}f^{'''} + \frac{(m+1)}{2}ff^{''} + m(1-f'^2) - \frac{\sigma_{thnf}/\sigma_f}{\rho_{thnf}/\rho_f}M(f'-1) = 0, \quad (2.\ 14)$$

$$\frac{1}{\mathrm{Pr}}\bigg(\frac{k_{thnf}/k_f}{(\rho C_p)_{thnf}/(\rho C_p)_f} + \frac{4}{3}\frac{\mathrm{Rd}}{(\rho C_p)_{thnf}/(\rho C_p)_f}\bigg)\theta'' + \frac{(m+1)}{2}f\theta' = 0. \quad (2.\ 15)$$

Rewriting equations 2. 14 and 2. 15 using simplified constants,

$$\frac{C_1}{C_2}f^{'''} + \frac{(m+1)}{2}ff^{''} + m(1-f'^2) - \frac{C_5}{C_2}M(f'-1) = 0, \quad (2.\ 16)$$

$$\frac{1}{\mathrm{Pr}}\bigg(\frac{C_3}{C_4} + \frac{4}{3}\frac{\mathrm{Rd}}{C_4}\bigg)\theta'' + \frac{(m+1)}{2}f\theta' = 0, \quad (2.\ 17)$$

The boundary conditions provided in equation 2. 8 are transformed as

$$\begin{cases} f(0) = S, \qquad f'(0) = \lambda, \quad \theta(0) = 1, \\ f'(\eta) \to 1, \qquad \theta(\eta) \to 0, \quad \text{as } \eta \to \infty. \end{cases} \quad (2.\ 18)$$

Here, the parameters such as the Prandtl number (Pr), the radiation parameter (Rd), the magnetic parameter (M), and the stretching/shrinking parameter (λ) are expressed as

$$\mathrm{Pr} = \frac{\nu_f}{\alpha_f}, \quad M = \frac{\sigma_f B_\circ^2}{\rho_f U_e}, \quad \mathrm{Rd} = \frac{4\sigma_\circ T_\infty^3}{k_f k^*}, \quad \lambda = \frac{U_w}{U_e},$$

$$C_1 = \frac{\mu_{thnf}}{\mu_f}, \quad C_2 = \frac{\rho_{thnf}}{\rho_f}, \quad C_3 = \frac{k_{thnf}}{k_f}, \quad C_4 = \frac{(\rho C_p)_{thnf}}{(\rho C_p)_f}, \ \text{ and } \ C_5 = \frac{\sigma_{thnf}}{\sigma_f}.$$

TABLE 2. Correlations for the ternary hybrid nanofluid by Jakeer et al. [18].

Properties	**Formula for ternary hybrid nanofluid**
Density	$\rho_{thnf} = (1-\phi_3)\left\{(1-\phi_2)\left[(1-\phi_1)\rho_f + \phi_1\rho_1\right] + \phi_2\rho_2\right\} + \phi_3\rho_3$
Heat Capacity	$(\rho C_p)_{thnf} = (1-\phi_3)\left\{(1-\phi_2)\left[(1-\phi_1)(\rho C_p)_f + \phi_1(\rho C_p)_1\right] + \phi_2(\rho C_p)_2\right\} + \phi_3(\rho C_p)_3$
Viscosity	$\frac{\mu_{thnf}}{\mu_f} = \frac{1}{(1-\phi_1)^{2.5}(1-\phi_2)^{2.5}(1-\phi_3)^{2.5}}$
Thermal Conductivity	$\frac{k_{thnf}}{k_{hnf}} = \frac{k_3+2k_{hnf}-2\phi_3(k_{hnf}-k_3)}{k_3+2k_{hnf}+\phi_3(k_{hnf}-k_3)}$, *where* $k_{hnf} = \frac{k_2+2k_{nf}-2\phi_2(k_{nf}-k_2)}{k_2+2k_{nf}+\phi_2(k_{nf}-k_2)} \times k_{nf}$ and $k_{nf} = \frac{k_1+2k_f-2\phi_1(k_f-k_1)}{k_1+2k_f+\phi_1(k_f-k_1)} \times k_f$
Electrical Conductivity	$\frac{\sigma_{thnf}}{\sigma_{hnf}} = \frac{\sigma_3+2\sigma_{hnf}-2\phi_3(\sigma_{hnf}-\sigma_3)}{\sigma_3+2\sigma_{hnf}+\phi_3(\sigma_{hnf}-\sigma_3)}$, *where* $\sigma_{hnf} = \frac{\sigma_2+2\sigma_{nf}-2\phi_2(\sigma_{nf}-\sigma_2)}{\sigma_2+2\sigma_{nf}+\phi_2(\sigma_{nf}-\sigma_2)} \times \sigma_{nf}$ and $\sigma_{nf} = \frac{\sigma_1+2\sigma_f-2\phi_1(\sigma_f-\sigma_1)}{\sigma_1+2\sigma_f+\phi_1(\sigma_f-\sigma_1)} \times \sigma_f$

In this case, the representation of the nanoparticles' volume fractions is ϕ_i $(i = 1, 2, 3)$., where the subscripts 1, 2, and 3 stand for SiO_2, TiO_2, and Al_2O_3 nanoparticles, respectively. The subscripts *thnf*, *hnf*, *nf*, and f stand for ternary hybrid nanofluid, hybrid nanofluid, nanofluid, and base fluid, respectively.

TABLE 3. Nanoparticles and base fluid thermophysical characteristics by Nasir et al. [32].

Thermophysical properties	SiO_2	TiO_2	Al_2O_3	H_2O
$\rho(kg/m^3)$	2270	4250	6310	997.1
$k(W/mK)$	1.4013	8.953	32.9	0.6071
$C_p(J/kgK)$	730	711	686.2	4179
σ(S/m)	10^{-12}	2.6×10^6	5.96×10^7	5.5×10^{-6}
ϕ	1%	1%	1%	—
Pr	—	—	—	6.2

To better understand the behavior and properties of the fluid under different conditions, Table 2 presents correlations for the ternary hybrid nanofluid. These correlations facilitate the determination of the nanofluid's temperature and flow characteristics, which are additionally applicable to general analysis.

Table 3 outlines the thermophysical properties of the nanoparticles and the base fluid. It presents key parameters essential for realistic modeling of ternary hybrid nanofluids in heat transfer and fluid flow applications. These parameters include density, absolute viscosity, specific heat, as well as thermal and electrical conductivity.

3. NEURAL NETWORK MODELING STRATEGY

The Levenberg-Marquardt technique, which combines the positive aspects of gradient descent with the Gauss-Newton method, is frequently used to train artificial neural networks. This approach makes neural network training quicker and more reliable. As a result, network parameters may be optimized effectively without running the risk of becoming trapped in local minima. Information shown here is the precise and dependable capacity to describe fluid dynamics utilizing intricate mathematical equations that need the intersection of numerous variables, producing valuable result predictions. This model is

known as LMBA-ANN. It can answer issues pertaining to temperature, velocity, and other fluid parameters since it can effectively manage nonlinear relationships.

The approach used in this study includes training employing the Levenberg-Marquardt algorithm, simulating neural networks, and numerically comparing the outcomes, as shown in Figure 4. A methodological framework, block-structured for a stepwise approach to data acquisition, model development, and problem formulation, is proposed as a brief systematic solution. Equations 2. 16 and 2. 17 were then simultaneously solved in the `bvp4c` numerical solver, subject to the boundary conditions in equation 2. 18 . The LMBA-ANN approach uses this numerical technique to reformulate the governing equations into a system of first-order ordinary differential equations (ODEs) for an input to the ANNs. Simulations of numerical experiments were carried out under the default setup of `bvp4c` for integration limits, required accuracy, termination conditions, etc.

The primary equations were solved with a step size of $\eta = 0.005$, ensuring convergence while maintaining an error tolerance of approximately zero. To simplify the analysis, equation 2. 18 imposed a limiting condition as $\eta \to 5$, avoiding the interval $[0, 5]$. This approach is particularly suited for analyzing fluids exhibiting significant variations in velocity and temperature profiles. The `bvp4c` solver efficiently rescaled the ODEs for these profiles, enabling accurate and reliable numerical solutions.

Next, a three-layer neural network is generated using the `bvp4c` method to provide the dataset, which is then used in a supervised learning framework using three layers trained with the Levenberg-Marquardt algorithm. The neural network architecture has two hidden layers of 10 neurons, with input and output layers. The controlling model is the `bvp4c` approach, used to produce the training data for the network. Three groups are randomly selected from the reference dataset: For training, validation, and testing, it is divided into 70%, 15%, and 15%. This includes 401 samples in total: 60 for validation, 60 for testing, and 281 for training. In a neural network made up of neurons, inputs are processed, intermediate output is produced at the output layer, and the middle output is the consequence of nonlinear changes inside the hidden layers. The computation of each hidden layer neuron is a weighted sum of its inputs, plus a bias, processed via a sigmoid activation function. The mathematical representation is given by:

$$\sum_{m=1}^{i} w_{mn} P_m + b_n, \quad k_n = \frac{1}{1 + e^{-z}},$$

The weights are represented by w_{mn}, the inputs by P_m, the bias by b_n, and the activated output of a neuron by k_n. Each weight w_{mn} defines the connection between the m-th neuron in the previous layer and the n-th neuron in the current layer. The bias term b_n helps adjust the activation threshold, while the neuron's output k_n is obtained after applying the activation function. To optimize the network's performance, the Levenberg-Marquardt training algorithm is employed. This algorithm fine-tunes the weights and biases by iteratively reducing the error between predicted and actual values, thereby enhancing accuracy. The training process continues until a predefined error threshold or fitness level is met. The effectiveness of the trained network is assessed using multiple error and accuracy metrics, including:

$$\text{MSE} = \frac{\sum_{j=1}^{i}(P_j - T_j)^2}{k}, \quad R = 1 - \frac{\sum_{j=1}^{i}(P_j - T_j)^2}{\sum_{j=1}^{i}(T_j - \bar{T}_j)^2},$$

where $\bar{T}_j$ indicates the mean of the target values, T_j gives the target value, and P_j denotes the predicted value. More accurate and dependable predictions are shown by lower MSE values and R-values nearer 1.

The design methodology consists of two distinct phases:

1. **Numerical Solution Using `bvp4c`:**

In the first phase, MATLAB's `bvp4c` solver, aimed at solving boundary value problems (BVPs) for ordinary differential equations (ODEs), is used. This method is applied to systems describing the behavior of fluid flow, such as flow rate and temperature characteristics. A particularly nice aspect of the `bvp4c` solver is that it will automatically stop once the solution has reached an accuracy that satisfies the user-defined accuracy requirements. It performs such computations dynamically, adapting its computations to meet accuracy objectives and reducing computational effort while remaining precise. This phase provides a reference dataset for the subsequent phase, which utilizes the numerical solution above as a test case for several wind turbine models developed using boundary layer turbulence models.

2. **Neural Network Training with `nftool`:**

In the second phase, I use MATLAB's Neural Network Toolbox (`nftool`) to train a 10 hidden layer multi-layer perceptron (MLP) neural network. The numerical solution provided by the `bvp4c` solver is used to get a training dataset.The reason for the adoption of the Levenberg-Marquardt Backpropagation Algorithm is because of its power in optimization, a merger of the Gradient Descent and Gauss-Newton Algorithm principles. This provides a mechanism for the network to pick up complex patterns and relationships in the data, as well as smaller errors. The neural network is able to be trained, after which the neural network becomes a powerful prediction instrument for the system's behavior based on learned patterns.

In this work, a two-phase strategy combining the precision of numerical solvers with the predictability of neural networks is presented, leading to a hybrid model. Furthermore, the design enhances solution quality and computational efficiency, particularly for complex flow systems.

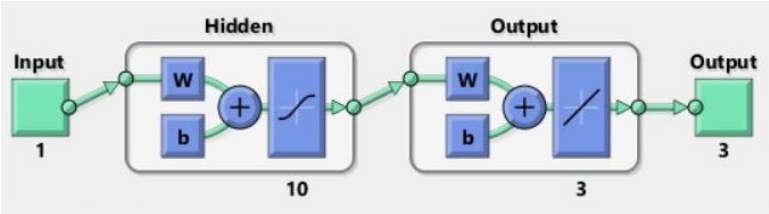

FIGURE 2. Neural network procedure for the proposed model.

The neural network depicted in Figures 2 and 3 has one input layer, two hidden layers, and one output layer. Three neurons, designated x_1, x_2, and x_3, comprise the input layer

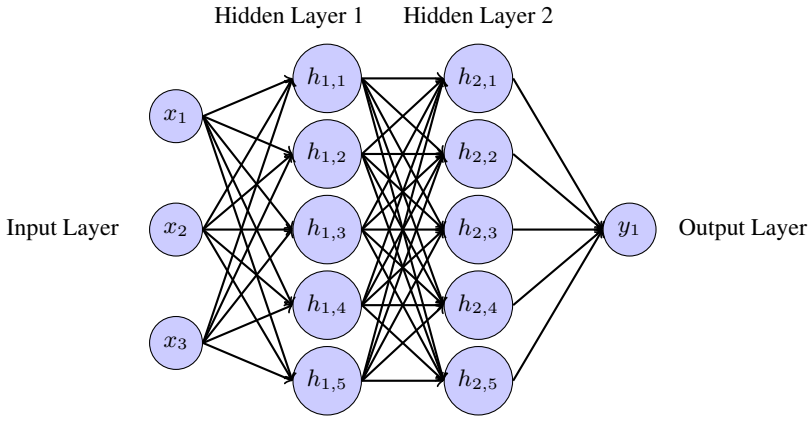

FIGURE 3. Neural network diagram with arrows entering and exiting from the sides of neurons.

and describe the input characteristics. The neurons in the very first hidden layer are totally linked to every neuron within the input layer. The two hidden layers, arranged sequentially, each contain five neurons, labeled as $h_{1,i}$ and $h_{2,i}$ ($i = 1, 2, \ldots, 5$), where the subscripts indicate the layer and neuron indices. These layers transform the inputs through successive computations. Finally, the output layer contains a single neuron, labeled y_1, which produces the network's final output. The connections across all layers represent the flow of information, with weighted links enabling the learning process.

The flow diagram illustrating the ternary hybrid nanofluid flow model, which gives a thorough summary of our investigation, is shown in Figure 4. It ensures consistency and clarity in the study presentation by emphasizing the crucial components and conclusions.

4. INTERPRETATION AND DISCUSSION OF RESULTS

The ranges of the controlling parameters (stretching/shrinking parameter λ, magnetic parameter M, suction/injection parameter S, wedge angle m, and radiation parameter R_d) are carefully selected to reflect realistic values encountered in engineering and industrial applications. The stretching/shrinking parameter λ represents surface motion in processes such as extrusion, film stretching, and moving belts; the moderate values considered (e.g., $\lambda = 0.5, 0.6, 0.8$) capture practical processing speeds where boundary-layer effects remain significant. The magnetic parameter M denotes the strength of Lorentz-force effects in electrically conducting fluids and the chosen values (e.g., $M = 1.0, 1.2, 1.6$) correspond to regimes often reported in MHD cooling, electromagnetic pumps, and flow control studies. The suction/injection parameter S reflects wall mass transfer in porous surface cooling and transpiration systems, with the selected values (e.g., $S = 0.1, 0.3, 0.7$) modeling weak-to-moderate suction or injection intensities that stabilize or destabilize the boundary layer without producing nonphysical reversal. The wedge-angle parameter m corresponds to geometric variations in diffusers, nozzles, and tapering channels; the values used (e.g., $m = 0.5, 0.7, 0.9$) represent both mildly and strongly converging/diverging

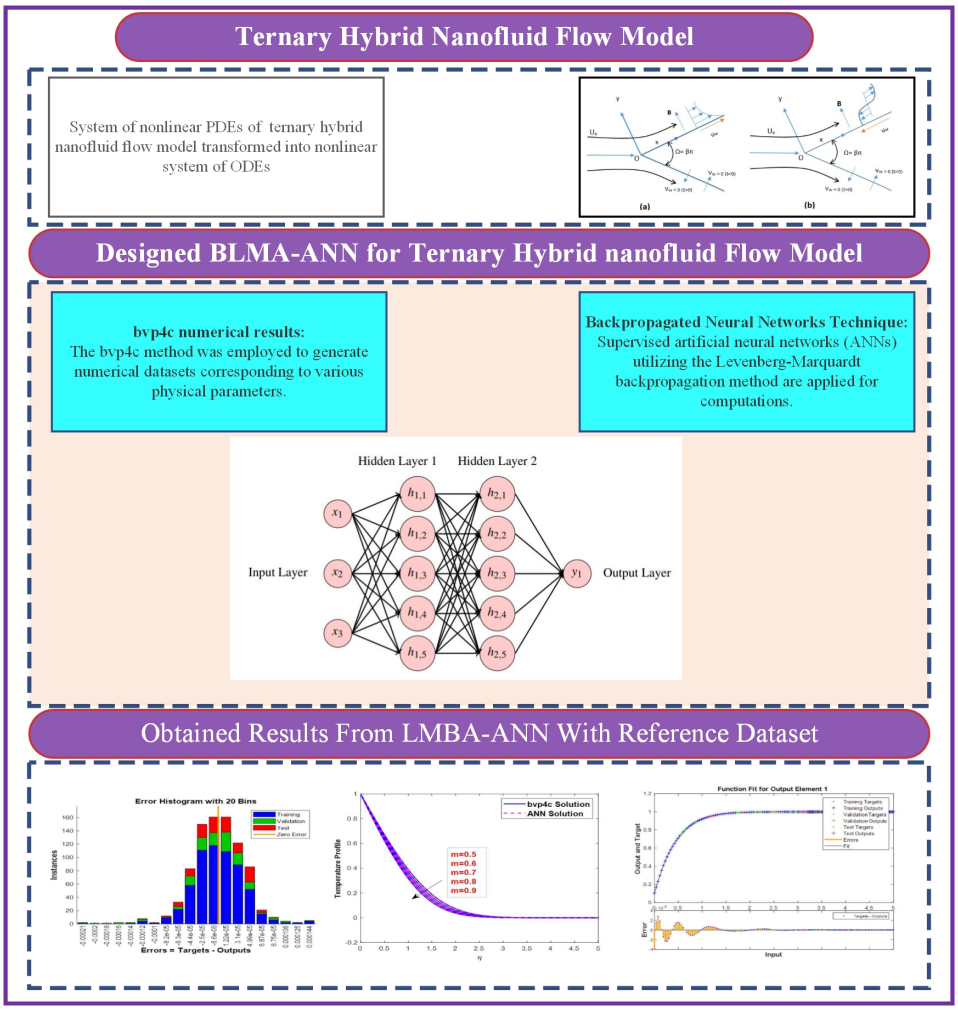

FIGURE 4. Flow diagram of the ternary hybrid nanofluid flow model.

configurations. Finally, the radiation parameter R_d accounts for thermal radiation in high-temperature systems such as solar receivers, combustion chambers, and high-power electronics, with the values considered (e.g., $R_d = 1.2, 2.2, 4.2$) spanning low-to-moderate radiative influence where radiation augments conduction and convection without dominating the energy transport. These parameter choices ensure that the numerical results remain physically meaningful and relevant to a wide range of industrial and engineering applications.

Table 5 provides a general comparison between the ANN-based approach and the traditional numerical solver `bvp4c`. The ANN model demonstrates high accuracy, rapid computation, and the ability to generalize across a wide parameter space after training.

TABLE 4. Variation of physical parameters for training and performance evaluation.

Parameter	Value	Case	MSE			Epoch	Time	Performance	Gradient	Mu
			Train	Valid	Test					
m	0.5	I	2.77×10^{-9}	2.25×10^{-9}	1.30×10^{-8}	262	3 s	2.77×10^{-8}	9.95×10^{-8}	1×10^{-8}
	0.7	II	4.71×10^{-7}	3.56×10^{-6}	1.06×10^{-8}	500	4 s	5.65×10^{-7}	3.44×10^{-6}	1×10^{-7}
	0.9	III	1.24×10^{-6}	2.12×10^{-7}	9.76×10^{-8}	900	5 s	5.27×10^{-7}	4.24×10^{-6}	1×10^{-6}
λ	0.5	I	2.13×10^{-9}	5.53×10^{-10}	8.16×10^{-9}	142	2 s	2.13×10^{-7}	9.94×10^{-8}	1×10^{-9}
	0.6	II	6.65×10^{-6}	2.55×10^{-7}	9.22×10^{-6}	1200	6 s	9.17×10^{-6}	2.10×10^{-5}	1×10^{-7}
	0.8	III	2.27×10^{-7}	1.12×10^{-6}	1.26×10^{-7}	1000	5 s	6.65×10^{-7}	3.33×10^{-6}	1×10^{-6}
M	1.0	I	6.33×10^{-7}	1.06×10^{-7}	2.80×10^{-7}	68	1 s	6.33×10^{-9}	1.80×10^{-6}	1×10^{-8}
	1.2	II	8.28×10^{-7}	3.14×10^{-7}	6.76×10^{-5}	600	4 s	1.48×10^{-7}	2.93×10^{-6}	1×10^{-6}
	1.6	III	1.83×10^{-6}	7.73×10^{-6}	3.33×10^{-6}	1000	5 s	7.30×10^{-9}	3.12×10^{-5}	1×10^{-7}
R_d	1.2	I	3.24×10^{-8}	1.75×10^{-8}	6.21×10^{-8}	63	1 s	3.24×10^{-8}	9.72×10^{-8}	1×10^{-8}
	2.2	II	2.43×10^{-7}	3.42×10^{-7}	9.43×10^{-6}	800	4 s	4.83×10^{-7}	3.45×10^{-6}	1×10^{-7}
	4.2	III	7.64×10^{-8}	9.65×10^{-6}	8.81×10^{-6}	600	4 s	3.62×10^{-7}	4.56×10^{-5}	1×10^{-6}
S	0.1	I	2.34×10^{-9}	3.14×10^{-9}	4.63×10^{-7}	242	3 s	2.34×10^{-7}	9.87×10^{-8}	1×10^{-8}
	0.3	II	5.28×10^{-6}	7.18×10^{-7}	4.29×10^{-6}	800	4 s	3.97×10^{-6}	1.10×10^{-5}	1×10^{-7}
	0.7	III	4.27×10^{-8}	8.13×10^{-6}	9.29×10^{-7}	900	5 s	2.83×10^{-7}	1.55×10^{-5}	1×10^{-6}

TABLE 5. General comparison of ANN (LMBA-based) with numerical solver (`bvp4c`).

Aspect	**ANN (LMBA-based)**	**Numerical Solver (bvp4c)**
Accuracy	Produces solutions with errors typically below 10^{-3} compared to reference results.	Highly accurate reference solutions but dependent on mesh refinement and solver tolerances.
Computational Cost	Once trained, provides rapid predictions for new parameter sets without repeated solving.	Requires fresh computation for every parameter change, increasing time cost.
Generality	Capable of generalizing across a broad parameter space after training.	Provides case-specific results; no direct generalization to unseen parameter values.
Robustness	Handles nonlinearities effectively and remains stable under wide parameter variations.	Robust for well-posed problems but may face convergence issues for stiff or highly nonlinear systems.
Data Efficiency	Learns from a limited set of numerical solutions and reuses knowledge for multiple predictions.	Requires full computation for each new case; no reuse of past results.
Scalability	Easily extendable to higher-dimensional parameter spaces and complex models.	Computationally expensive for large-scale or multi-parameter studies.

In contrast, `bvp4c` delivers highly accurate case-specific solutions but requires repeated computations for new parameters. Overall, the table highlights the efficiency, robustness, and scalability advantages of the ANN approach for solving complex differential systems.

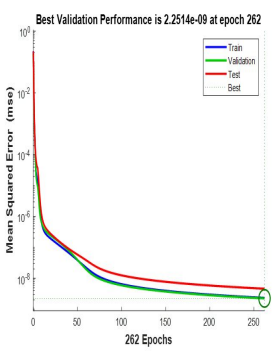

(A) Validation Performance.

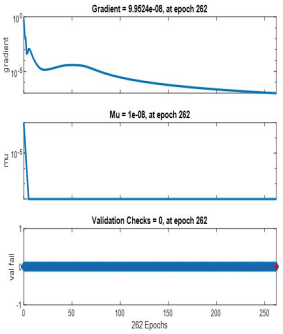

(B) Gradient, Mu, Validation checks.

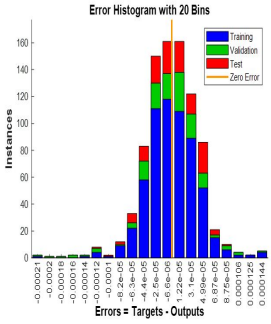

(C) Error Histogram.

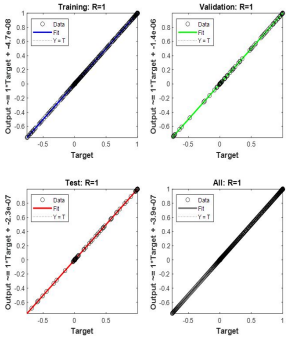

(D) Regression analysis.

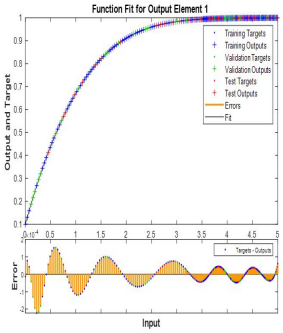

(E) Function fitting graph.

FIGURE 5. Effect of Parameter "m" on Flow Behavior: LMBA Data Analysis for Case 1.

Equations. 2. 16 , 2. 17 , and 2. 18 govern the ternary hybrid nanofluid flow model, which is computed using the Levenberg-Marquardt backpropagation algorithm (LMBA) and the results are examined. The data for three distinct situations are displayed in Table 4 in order to investigate the effects of various parameters on temperature and velocity profiles. Furthermore, the stretching parameter is represented by λ, the magnetic parameter by M, the suction parameter by S, the wedge angle by m, and the radiation parameter by Rd. Understanding how each of these factors affects the temperature and velocity profiles is crucial to comprehending way the ternary hybrid nanofluids react to the flow domain. These parameters all have a major influence on the flow characteristics.

For velocity and temperature profiles, the reference dataset is generated using the MATLAB bvp4c numerical method, which is employed to solve the ternary hybrid nanofluid flow model over the domain η ranging from 0 to 5. This analysis is conducted for three distinct cases, each involving different parameter values, within the framework of the Levenberg-Marquardt Backpropagation Algorithm (LMBA) in conjunction with artificial

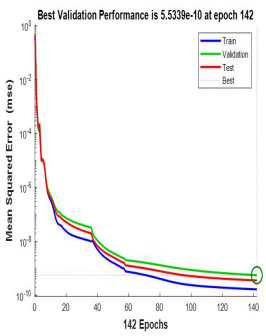

(A) Validation Performance.

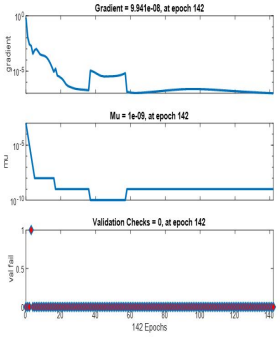

(B) Gradient, Mu, Validation checks.

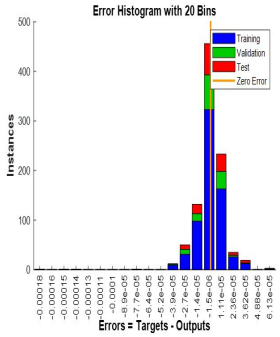

(C) Error Histogram.

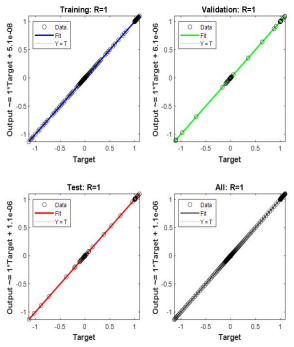

(D) Regression analysis.

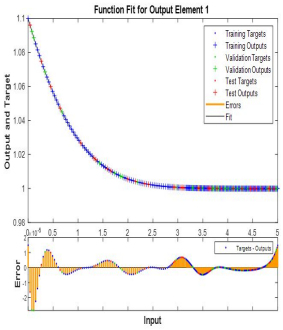

(E) Function fitting graph.

FIGURE 6. Effect of Parameter "λ" on Flow Behavior: LMBA Data Analysis for Case 1.

neural networks. In this process, the ternary hybrid nanofluid flow model is solved by the LMBA leverages the MATLAB nftool. The dataset for the velocity and temperature profiles is structured into three subsets: The dataset is divided such that 70 % is used for training the neural network, 15 % is set aside for validation, and the remaining 15 % is utilized for evaluating the model's performance.

Figures 5, 6, and 7 illustrate the LMBA data analysis for parameters such as the wedge angle m, stretching/shrinking parameter λ, and magnetic parameter M in Case 1. Panels 5(A)–9(A) display the validation performance results for the first case under different values of these parameters. Panels 5(B)–9(B) show the gradient, Mu, and validation checks for the same cases. Further analysis, shown in Figures 8 and 9, highlights the LMBA data analysis for the radiation parameter Rd and the suction/injection parameter S in Case 1. The error histograms for each case, illustrating the LMBA results, are presented in Figures 5(C)–9(C), while the regression analysis results are displayed in Figures 5(D)–9(D).

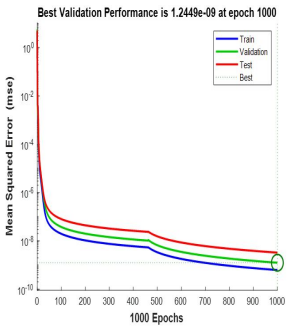

(A) Validation Performance.

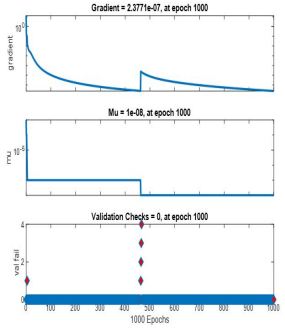

(B) Gradient, Mu, Validation checks.

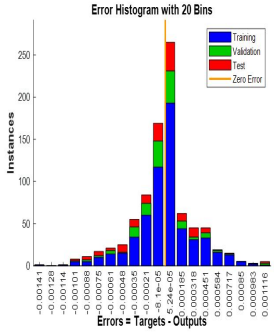

(C) Error Histogram.

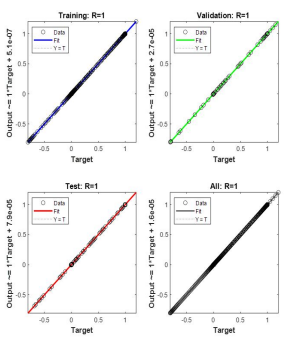

(D) Regression analysis.

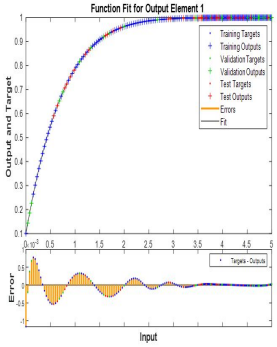

(E) Function fitting graph.

FIGURE 7. Effect of Parameter "M" on Flow Behavior: LMBA Data Analysis for Case 1.

Table 4 provides a summary of the mean squared error (MSE) convergence for training, testing, and validation. Figures 5(A)–9(A) illustrate the MSE convergence plots, indicating that the best performance is achieved at specific epochs [262, 142, 1000, 63, and 242] with corresponding MSE values of approximately $[2.251 \times 10^{-9},\ 5.5339 \times 10^{-10},\ 1.2449 \times 10^{-9},\ 1.7511 \times 10^{-8},\ 3.1377 \times 10^{-9}]$. The gradient values and Mu parameters for the Levenberg-Marquardt backpropagation algorithm are recorded as $[2.5997 \times 10^{-5},\ 9.941 \times 10^{-8},\ 1.7992 \times 10^{-6},\ 9.7197 \times 10^{-8},$
$9.8706 \times 10^{-8}]$ and $[1 \times 10^{-7},\ 1 \times 10^{-9},\ 1 \times 10^{-8},\ 1 \times 10^{-8},\ 1 \times 10^{-8}]$, respectively, as depicted in Figures 5(B)–9(B). These results highlight the convergence efficiency and the precision achieved by the LMBA across various cases.

Across all situations, the error histograms for Case 1 show that the difference between the output and the network's aim is almost insignificant. The errors are approximately $[-3.7 \times 10^{-5},\ -1.5 \times 10^{-6},\ 5.24 \times 10^{-5},\ -1.3 \times 10^{-5},\ -6.6 \times 10^{-6}]$, closely aligned with the reference zero-line error bin, as depicted in Figures 5(C)–9(C). Furthermore, the

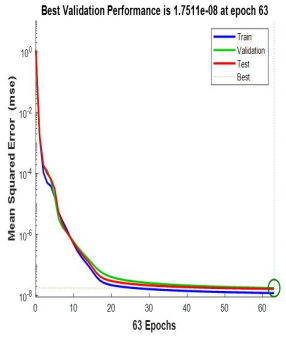

(A) Validation Performance.

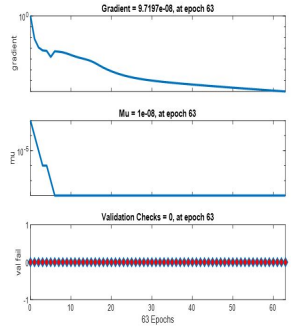

(B) Gradient, Mu, Validation checks.

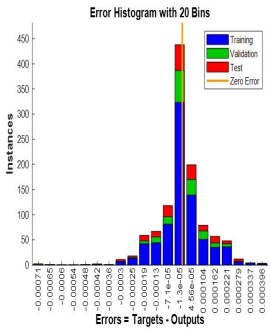

(C) Error Histogram.

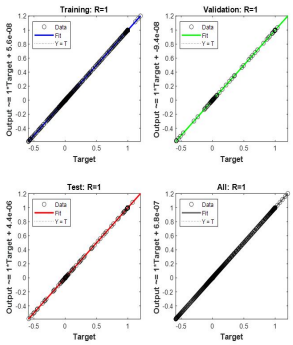

(D) Regression analysis.

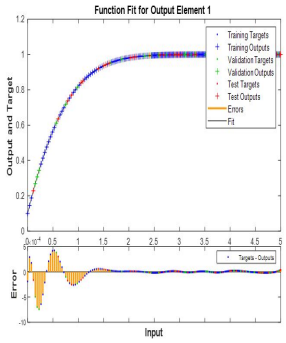

(E) Function fitting graph.

FIGURE 8. Effect of Parameter "Rd" on Flow Behavior: LMBA Data Analysis for Case 1.

regression analysis, shown in Figures 5(D)–9(D), demonstrates a strong correlation between the predicted and target values, with R-values nearing 1. This demonstrates the model's exceptional accuracy and reliability in predicting the velocity profile for the ternary hybrid nanofluid flow system.

The fitness graphs for each case, shown in 5(E)–9(E), illustrate the correlation between the target and output values across the training, validation, and testing phases, with errors minimized to the order of 10^{-5} per unit time. For Case 1, the fitness graphs for all scenarios, as shown in Figures 5(E) – 9(E), reveal a consistent alignment between the target and the results for each step of the process. Dots $(\cdot)$ represent the target values, while plus signs $(+)$ denote the outcomes of training, testing, and validation, further emphasizing the accuracy of the model.

4.1. **Influence of Streamline Patterns on Flow Dynamics.** Streamlines represent the trajectories that fluid particles follow in a steady flow, and are defined such that they are

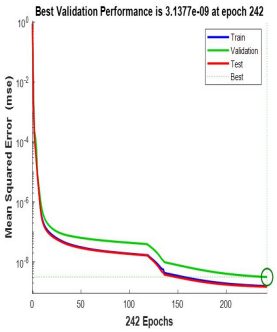

(A) Validation Performance.

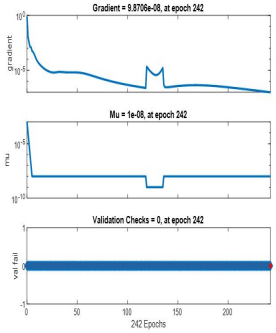

(B) Gradient, Mu, Validation checks.

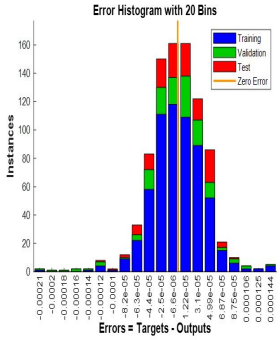

(C) Error Histogram.

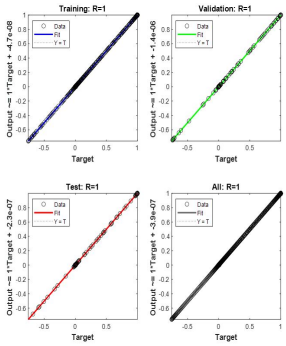

(D) Regression analysis.

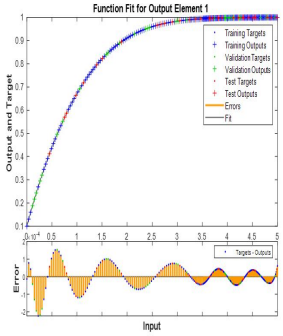

(E) Function fitting graph.

FIGURE 9. Effect of Parameter "*S*" on Flow Behavior: LMBA Data Analysis for Case 1.

everywhere tangent to the local velocity vector field. In the present analysis, streamline plots are incorporated to visualize the flow behavior of the ternary hybrid nanofluid under the influence of key parameters. These plots provide a clear depiction of the velocity distribution and help illustrate regions of acceleration, deceleration, and flow circulation, thereby offering valuable physical insight beyond the velocity profile alone.

In Figure 10(A), the surface flow emerging from the surface of a shell in a surface plot is visualized to represent the fluid flow behavior over the surface. The streamlines give the path taken by a fluid particle, helping describe the nature of the flow. This is enhanced with the surface plot, which shows the three-dimensional flow structure, providing insight into how the flow is behaving in relation to the surface.

The streamlines are shown without the surface plot in Figure 10(B). This visualization only shows the pattern of flow, making it easier to understand how the fluid flows in the two-dimensional plane. The velocity distribution of the fluid can be understood from the

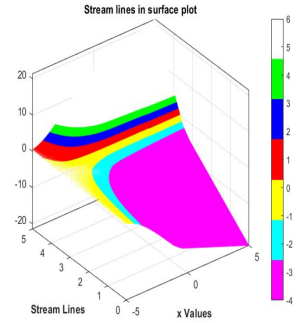

(A) Stream lines in surface plot.

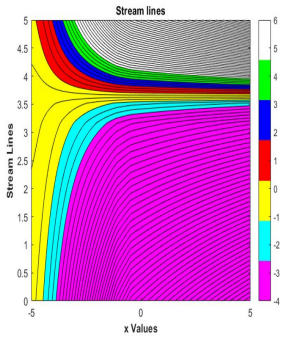

(B) Stream lines.

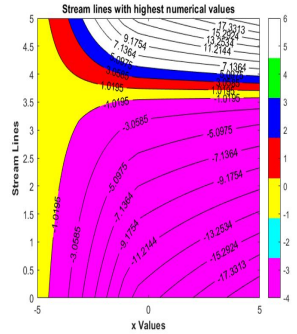

(C) Stream lines with numerical values.

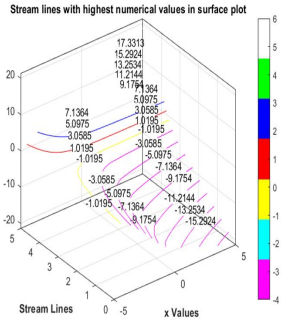

(D) Stream lines with numerical values in surface plot.

FIGURE 10. Stream lines results.

density and curvature of the streamlines; closely spaced streamlines represent regions of high velocity.

The numerical values of the magnitude of the velocity field at different locations of the flow are shown in figure 10(C) by the streamlines. The numerical values included add quantitative information to the flow characteristics, especially about velocity variations across the flow domain.

Figure 10(D) shows the streamlines and numerical values in a surface plot. They offer a combination of visual and numerical data, giving complete information of flow dynamics and simultaneously describing the overall flow structure and the precise velocity magnitudes. While visually attractive, streamline visualization generally provides only 2D information; the surface plot helps to add depth to the visualization by giving a 3D perspective on the streamline plot that can be particularly valuable for analyzing complicated flow patterns involving variable boundary conditions or additional physical effects (radiation, magnetic fields, etc.).

4.2. **Impact of parameter variations on velocity and temperature profiles.** The thermal performance of ternary hybrid nanofluids (THNFs) has been observed to surpass that of conventional nanofluids (NFs) and hybrid nanofluids (HNFs). This enhancement is primarily due to the synergistic effects of combining three different nanoparticles, which improve thermal conductivity, heat transfer rates, and dispersion stability. As shown in Table 6, ternary hybrid nanofluids exhibit higher thermal conductivity and heat transfer enhancements compared to conventional and hybrid nanofluids, confirming their superior performance and stability.

TABLE 6. Comparative performance of ternary hybrid nanofluids with conventional nanofluids and hybrid nanofluids.

Nanofluid Type	Thermal Conductivity Enhancement (%)	Heat Transfer Enhancement (%)	Stability	Remarks
Conventional NF baseline performance	0–10	0–25	Moderate	Single nanoparticle;
Hybrid NF moderate enhancement	5–15	15–50	Improved	Two nanoparticles;
Ternary Hybrid NF synergistic effect leads to superior thermal performance	10–20	40–80	High	Three nanoparticles;

Figure 11(A) displays the effect of the stretching/shrinking parameter (λ) on the velocity profile. The velocity of the fluid raises as λ enhances. The parameter, λ, controls the speed of stretching or shrinking of the surface. When the surface is stretched, a force is applied to the fluid along the surface, pulling the fluid in the same direction. This results in an increase in the fluid's velocity near the surface. As λ grows, the stretching effect is more pronounced, so forcing particles to move faster between the surfaces. As a result, the velocity profile is steeper, which means a higher flow rate near the surface. This behavior arises from an increase in λ increasing the stretching force, which aids in fluid motion, leading to a thinner boundary layer. This subsequently increases the velocity of the fluid at the surface. Conversely, decreasing λ (or equivalently shrinking) would reverse this, slowing the flow and growing the thickness of the boundary layer. The raise in velocity with raising λ also has important implications for heat transfer. Consequently, with a rise in the velocity of the fluid, convective heat transfer improves because the faster-flowing fluid can effectively remove heat farther away from the surface. The reason for this balanced behavior is highly important in systems where efficient heat dissipation is essential, such as in cooling applications or heat exchanger systems. As an outcome, the enhancement in velocity is because of steeper λ, which raises the fluid motion and heat transfer, and hence the stretching parameter has an important role in governing these phenomena.

The impact of the wedge angle parameter (m) on the velocity profile is illustrated in Figure 11(B). The velocity of the fluid rises as (m) enhances. As (m) increases, the fluid

velocity also rises. A steeper wedge angle exerts a greater force along the fluid surface, leading to an increase in the fluid's velocity near the surface. Consequently, the velocity profile is higher, particularly close to the surface. This occurs because, as the wedge narrows, the fluid is forced through a smaller channel, compressing and accelerating to maintain flow continuity. In applications involving wedge-shaped geometries, the velocity is highly sensitive to changes in (m), as the wedge angle can be adjusted to regulate the flow. Beyond enhancing velocity, increasing (m) also improves heat transfer characteristics due to the faster-moving fluid, which enhances convective heat transport. This behavior is particularly significant in cooling or heating systems.

Figure 11(C) illustrates the velocity profile under the influence of the magnetic parameter (M). The velocity of the fluid declines with an increase of M. The applied magnetic field generates the Lorentz force; it is the resistive force acting perpendicularly to the velocity and its direction of the magnetic field, respectively. This resistive force raises as M enhances, slowing the motion of the fluids. The Lorentz force resists the flow, dampening the velocity, in particular when the magnetic field is the strongest. It results in a reduction of the velocity profile, particularly close to the surface, where the magnetic effects are most important. The flow speed can be adjusted by the use of a higher magnetic parameter in systems where the motion of the fluid needs to be controlled precisely, as in the case of MHD pumps or heat exchangers with the use of magnetic fields for flow enhancement.

Figure 11(D) shows the velocity profile as an expression of the suction/injection parameter (S). The constant mass flow parameter in this case is represented by $S = f(0)$. When $S > 0$, the fluid undergoes suction and injection when $S < 0$. The fluid's velocity grows as S rises. For a positive S value, there is a physical association with fluid suction (the same effect as of the fluid suction, which would enhance flow towards the surface, thereby increasing the velocity of the fluid). Larger S means increasing suction pulling harder on the free fluid and therefore higher velocity of fluid in the boundary layer. For example, if S becomes negative (fluid injection), the velocity near the surface dies off as the included surface is servicing a source or sink of fluid. S fluid suction is furthermore enhanced, and velocity is as well. This shows that the velocity profile becomes dependent on the mass flux parameter (S), where suction (positive S) generally increases flow velocity in the wall surface region.

Figure 12(A) visualizes the impact of the wedge angle m upon the temperature profile. In the case where the value of m improves, the temperature of the fluid also decreases. The wedge angle determines how much the fluid is stretched or shrunk. This leads to the fluid cooling faster when being stretched, thereby reducing the near surface temperature. Higher stretching rates of the fluid due to a larger wedge angle m physically lead to enhanced heat dissipation from the fluid, resulting in a reduced temperature. This effect is very important when the temperature of the fluid is a parameter of prime importance in heat transfer applications. Consequently, an increase in the parameter m leads to a shrinkage in the temperature profile, signifying a cooling effect caused by greater stretching of the fluid.

The influence of the magnetic field strength (M) on the temperature profile is shown in Figure 12(B). As M increases, the fluid temperature also rises. A stronger magnetic field is generated with higher M, which exerts a greater resistive force on the movement of the electrically conducting fluid, thereby increasing heat generation. A stronger magnetic field had led to higher viscous dissipation in the fluid, thereby raising the temperature in

the fluid. Additionally, the magnetic field's ability to impede fluid movement enhances the fluid's ability to retain thermal energy. The temperature rises, or there is a heating impact as a result of the magnetic parameter's (M) rising magnitude. A boundary layer's temperature profile must be controlled in order to improve the efficiency of heat and fluid flow transmission.

Figure 12(C) illustrates the temperature profile in relation to the radiation parameter Rd. The fluid temperature increases with higher values of Rd. Increases in the radiation parameter yield higher radiative heat flux, aiding the thermal energy in the fluid. The grow in this temperature profile thus occurs. However, at larger values of Rd, radiation becomes more important, resulting in higher temperatures because of the additional heat added through the radiative source. As such, in applications involving high radiation levels, or in high-temperature applications where radiation significantly impacts the heat transfer dynamics, higher radiation levels produce a very large increase in temperature.

Figure 13 shows the velocity and temperature profiles for ternary hybrid nanofluids, hybrid nanofluids, and simple nanofluids. Hybrid nanofluids and simple nanofluids exhibit lower velocity compared to ternary hybrid nanofluids. This occurs because the combined effects of multiple nanoparticles improve the thermal properties and reduce the fluid's drag. Hybrid nanofluid shows intermediate velocity because it possesses improved thermal conductivity than simple nanofluid and is reduced than that of ternary hybrid nanofluid. Simple nanofluids have the lowest velocity because of the relatively limited heat transfer they have to offer. In the temperature profile, ternary hybrid nanofluids present a steeper gradient of temperature, suggesting better heat dissipation. Synergistic effects of multiple nanoparticles in ternary hybrid nanofluids cause a significantly enhanced thermal conductivity. The temperature gradient of hybrid nanofluids is enhanced slightly as compared to that of simple nanofluids, which reflects their hybrid-enhanced thermal performance. However, simple nanofluids are found to have the least temperature gradient, as in the case of a single nanoparticle, which provided little improvement in thermal conductivity. These findings clearly indicate that in the context of nanofluids, the addition of more than one nanoparticle improves the velocity and temperature profiles, thereby enhancing the thermal conductivity and mechanisms of energy transport.

The influence of the controlling parameters is not only significant from a theoretical standpoint but also directly relevant to engineering applications. Variations in the wedge-angle parameter m reveal that larger angles promote flow divergence, weakening boundary-layer adhesion and consequently reducing cooling effectiveness. This behavior is critical in the design of diffusers and nozzles, where excessive divergence can lead to thermal inefficiency and undesirable recirculation. In contrast, smaller wedge angles stabilize the flow field, resulting in more uniform cooling performance and reduced thermal stresses, which are advantageous in microchannel cooling and compact heat-exchanger systems. Similarly, the magnetic parameter M demonstrates the well-known damping effect of the Lorentz force: increasing M suppresses fluid motion, which lowers convective heat transfer but enhances flow controllability. This has practical importance in electromagnetic pumps, liquid-metal cooling systems, and MHD-based flow regulation devices, where precise flow control may be prioritized over maximum heat removal. By linking these parametric effects to real-world outcomes, the results highlight the dual role of wedge geometry and

magnetic field strength in optimizing both cooling efficiency and flow management in advanced thermal-fluid systems.

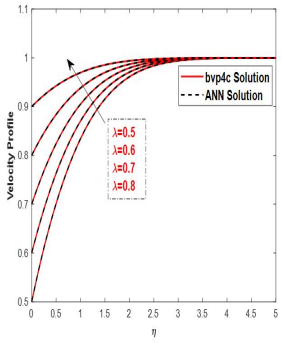

(A) Influence of parameter λ on velocity profile.

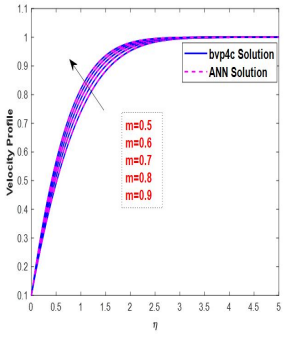

(B) Influence of parameter m on velocity profile.

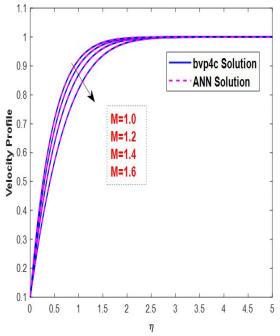

(C) Variation of velocity profile with parameter M.

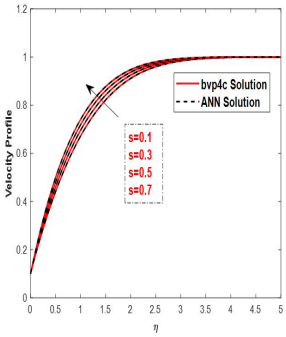

(D) Impact of parameter S on velocity profile.

FIGURE 11. Influence of different parameters on velocity profile.

5. CONCLUSION

Levenberg-Marquardt backpropagation algorithm-optimized artificial neural networks are implemented to study the ternary hybrid nanofluid flow model. The study focuses on essential parameters, such as the radiation parameter Rd, suction/injection parameter S, wedge angle m, magnetic parameter M, and stretching/shrinking parameter λ. The bvp4c solver effectively addresses inconsistencies in the model by generating a reference dataset. The Levenberg Marquardt method ensures high accuracy and alignment between the reference and predicted results. The dataset is divided into 70% for training, with the remaining 15% each allocated for testing and validation. The proposed approach's reliability and robustness are confirmed through performance metrics such as regression

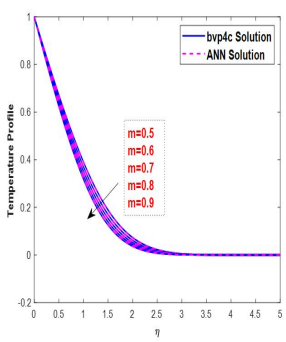

(A) Influence of m on temperature profile.

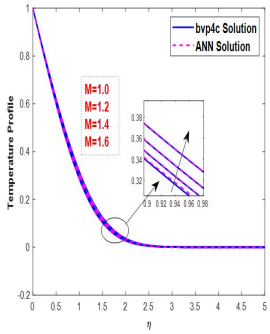

(B) Impact of M on temperature profile.

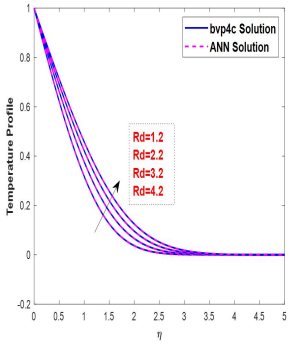

(C) Effect of Rd on temperature profile.

FIGURE 12. Influence of different parameters on temperature profile.

analyses, mean square error, convergence curves, and error histograms. The key findings of the study are concluded as follows:

- A hybrid computational approach integrating the Levenberg-Marquardt backpropagation algorithm with artificial neural networks (LMBA-ANN) was employed to solve the nonlinear differential equations efficiently.
- The optimal LMBA-ANN design at epoch 142 demonstrates a high level of accuracy, with a mean squared error (MSE) of 5.5339×10^{-10} and a perfect regression coefficient (R) of 1, indicating a strong correlation between the predicted and actual results.
- The ANN model was trained and validated using numerical solutions obtained from the bvp4c solver, achieving high accuracy as evidenced by regression analysis and error histograms.
- The critical value for thermal solutions decreased with an increase in the wedge angle parameter, highlighting its influence on the system's thermal behavior.

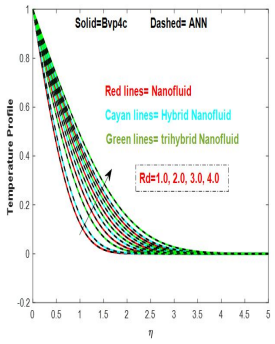

(A) Temperature profile of various kinds of fluids.

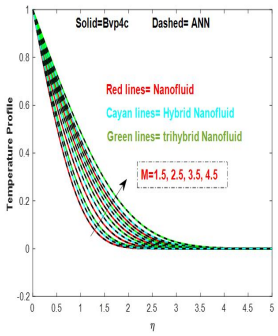

(B) Temperature profile of various kinds of fluids.

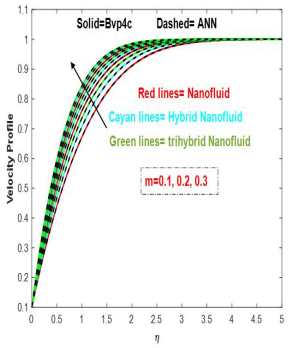

(C) Velocity profile of various kinds of fluids.

FIGURE 13. Velocity and temperature profiles of various kinds of nanofluids under varying various parameter.

- Compared to the conventional nanofluids, the heat transfer rate of the ternary hybrid nanofluid was relatively enhanced, with radiation further enhancing heat transfer efficiency.
- The results indicate that solutions are valid up to certain levels of stretching/shrinking and suction intensities, providing insights into flow stability under varying boundary conditions.
- The combination of numerical solvers and neural networks demonstrated significant improvements in computational efficiency and accuracy for ternary hybrid nanofluid flow models.
- The streamlines are visualized in various forms, including surface plots showing the three-dimensional flow structure, two-dimensional flow patterns, streamlines with numerical values representing velocity distribution, and a combination of both

streamlines and numerical values in surface plots, providing a comprehensive understanding of the flow dynamics and velocity magnitudes.

Future studies can leverage artificial intelligence, particularly the Levenberg-Marquardt Backpropagation Algorithm, to enhance the predictive capabilities of ternary hybrid nanofluid flow models. Integrating artificial intelligence into fluid dynamics applications can significantly enhance simulation accuracy, facilitate real-time analysis, and provide more precise modeling of complex interactions.

TABLE 7. **Nomenclature**

Symbol	**Name**	**Symbol**	**Name**
Rd	Radiation parameter	θ	Dimensionless fluid temperature
$\phi_1,\ \phi_2,\ \phi_3$	Nanoparticles concentrations	μ	Dynamic viscosity
ν	Kinematic viscosity	k^*	Coefficient of mean absorption
ρ_f	Density of fluid	C_p	Heat capacity
η	Similarity transformation	λ	Stretching/shrinking parameter
f (Subscript)	Base fluid	hnf (Subscript)	Hybrid nanofluid
$thnf$ (Subscript)	Ternary hybrid nanofluid	M	Magnetic parameter
S	Suction/injection parameter	k	Thermal conductivity
σ	Electrical conductivity	Pr	Prandtl number
ρ_1, ρ_2	Density of nanoparticles	T	Temperature of hybrid nanofluid
u	Fluid velocity in x-direction	β	Hartree pressure gradient parameter
v	Fluid velocity in y-direction	$u_w(x)$	Stretching/shrinking velocity
x, y	Cartesian coordinates	$\mathrm{B}_\circ$	Magnetic field strength
$U_e,\ U_w$	Constants	$u_e(x)$	Free stream velocity
Ω	Wedge's total angle	m	Wedge angle
$\sigma_\circ$	Stefan-Boltzmann constant	q_r	Radiative heat flux
q_w	Heat flux from the wedge surface		

Table 7 provides the nomenclature used throughout the study, listing the symbols and their corresponding definitions. This table ensures accuracy and uniformity in the depiction of the mathematical frameworks and equations by acting as a reference for comprehending the numerous parameters and variables employed throughout the analysis.

Acknowledgments: All the authors are obliged and thankful to the University of Management and Technology, Lahore, Pakistan, for facilitating and supporting the research work.

Author's Contributions: Writing-original draft preparation, Formal analysis, Problem formulation: Abdul Wahab and Saraj Khan; Investigation, Methodology, Supervision, Resources, Validation: Muhammad Imran Asjad, Abdul Wahab; Graphical discussion, Software, Review and editing: Saraj Khan and Abdul Wahab. All authors have read and agreed to the published version of the manuscript.

Funding: This research received no external funding.

Data Availability: Data sharing is not applicable to this article as no data sets were generated or analyzed during the current study.

Conflicts of interest: The authors declare that they have no conflicts of interest.

REFERENCES

[1] O. I. Abiodun, A. Jantan, A. E. Omolara, K. V. Dada, N. A. Mohamed, and H. Arshad, State-of-the-art in artificial neural network applications: A survey, Heliyon **4**, No. 11 (2018) e00938.

[2] H. Adun, I. Wole-Osho, E. C. Okonkwo, O. Bamisile, M. Dagbasi, and S. Abbasoglu, A neural network-based predictive model for the thermal conductivity of hybrid nanofluids, Int. Commun. Heat Mass Transf. **119**, No. 1 (2020) 104930.

[3] S. Agatonovic-Kustrin and R. Beresford, Basic concepts of artificial neural network (ANN) modeling and its application in pharmaceutical research, J. Pharm. Biomed. Anal. **22**, No. 5 (2000) 717–727.

[4] M. S. Alam, M. A. Khatun, M. M. Rahman, and K. Vajravelu, Effects of variable fluid properties and thermophoresis on unsteady forced convective boundary layer flow along a permeable stretching/shrinking wedge with variable Prandtl and Schmidt numbers, Int. J. Mech. Sci. **105**, No. 1 (2016) 191–205.

[5] F. M. Ali, R. Nazar, N. M. Arifin, and I. Pop, MHD stagnation-point flow and heat transfer towards stretching sheet with induced magnetic field, Appl. Math. Mech. **32**, No. 4 (2011) 409–418.

[6] I. S. Awaludin, A. Ishak, and I. Pop, On the stability of MHD boundary layer flow over a stretching/shrinking wedge, Sci. Rep. **8**, No. 1 (2018) 1–8.

[7] R. C. Bataller, Radiation effects in the Blasius flow, Appl. Math. Comput. **198**, No. 1 (2008) 333–338.

[8] M. Haris Butt, M. Imran Asjad, M. Armaghan Sadiq, and A. Hussanan, Study of ternary nanoparticles in Oldroyd-B fluid using ethylene glycol, Punjab Univ. J. Math. **56**, No. 12 (2024) 781–798.

[9] S. U. Choi, Enhancing thermal conductivity of fluids with nanoparticles, ASME Int. Mech. Eng. Congr. Expo. **17421**, No. 1 (1995) 99–105.

[10] S. A. Devi and S. S. U. Devi, Numerical investigation of hydromagnetic hybrid Cu–Al_2O_3/water nanofluid flow over a permeable stretching sheet with suction, Int. J. Nonlinear Sci. Numer. Simul. **17**, No. 5 (2016) 249–257.

[11] O. S. Eluyode and D. T. Akomolafe, Comparative study of biological and artificial neural networks, Eur. J. Appl. Eng. Sci. Res. **2**, No. 1 (2013) 36–46.

[12] M. F. Endalew and S. Sarkar, Numerical exploration of forced convection hydromagnetic hyperbolic tangent nanofluid flow over a permeable wedge with melting heat transfer, Sci. Rep. **13**, No. 1 (2023) 3515.

[13] S. K. Ghosh, O. Anwar Bég, and J. Zueco, Hydromagnetic free convection flow with induced magnetic field effects, Meccanica **45**, No. 2 (2010) 175–185.

[14] T. Hayat and S. Nadeem, Heat transfer enhancement with Ag–CuO/water hybrid nanofluid, Results Phys. **7**, No. 1 (2017) 2317–2324.

[15] T. Hayat, S. Nadeem, and A. U. Khan, Rotating flow of Ag–CuO/H_2O hybrid nanofluid with radiation and partial slip boundary effects, Eur. Phys. J. E **41**, No. 6 (2018) 75.

[16] R. U. Haq, S. Nadeem, Z. H. Khan, and N. S. Akbar, Thermal radiation and slip effects on MHD stagnation point flow of nanofluid over a stretching sheet, Physica E **65**, No. 1 (2015) 17–23.

[17] M. Ishaq, G. Ali, S. I. A. Shah, Z. Shah, S. Muhammad, and S. A. Hussain, Nanofluid Film Flow of Eyring Powell Fluid with Magneto Hydrodynamic Effect on Unsteady Porous Stretching Sheet, Punjab Univ. J. Math. **51**, No. 3 (2019) 147–169.

[18] S. Jakeer, S. R. R. Reddy, A. M. Rashad, M. L. Rupa, and C. Manjula, Nonlinear analysis of Darcy–Forchheimer flow in EMHD ternary hybrid nanofluid (Cu–CNT–Ti/water) with radiation effect, Forces Mech. **10**, No. 1 (2023) 100177.

[19] W. Jamshed, Numerical investigation of MHD impact on Maxwell nanofluid, Int. Commun. Heat Mass Transf. **120**, No. 1 (2021) 104973.

[20] S. U. Jan, U. Khan, M. Abd El-Rahman, S. Islam, A. M. Hassan, and A. Ullah, Effect of variable thermal conductivity of ternary hybrid nanofluids over a stretching sheet with convective boundary conditions and magnetic field, Results Eng. **20**, No. 1 (2023) 101531.

[21] M. Jawad, K. Shehzad, R. Safdar, and S. Hussain, Novel computational study on MHD flow of nanofluid flow with gyrotactic microorganism due to porous stretching sheet, Punjab Univ. J. Math. **52**, No. 12 (2020) 43–60.

[22] S. Khan, M. I. Asjad, M. B. Riaz, T. Muhammad, and M. N. Aslam, Innovative thermal management in the presence of ferromagnetic hybrid nanoparticles, Sci. Rep. **14**, No. 1 (2024) 18203.

[23] S. Khan, M. I. Asjad, and F. Maiz, Artificial neural networks computing for heat transfer flow of hybrid nanofluid in rectangular geometry, Comput. Biol. Med. **194**, No. 1 (2025) 110475.

[24] U. Khan, N. Ahmed, S. T. Mohyud-Din, and B. Bin-Mohsin, Nonlinear radiation effects on MHD flow of nanofluid over a nonlinearly stretching/shrinking wedge, Neural Comput. Appl. **28**, No. 8 (2017) 2041–2050.

[25] K. Kumar and G. S. M. Thakur, Advanced applications of neural networks and artificial intelligence: A review, Int. J. Inf. Technol. Comput. Sci. **4**, No. 6 (2012) 57–68.

[26] M. Kumari, H. S. Takhar, and G. Nath, MHD flow and heat transfer over a stretching surface with prescribed wall temperature or heat flux, Heat Mass Transf. **25**, No. 6 (1990) 331–336.

[27] Y. Li, B. Shen, H. Yan, S. K. Boetcher, and G. Xie, Heat transfer enhancement of rotating wedge-shaped channels with pin fins and Kagome lattices, Numer. Heat Transf. Part A Appl. **77**, No. 12 (2020) 1014–1033.

[28] B. Mahanthesh, J. Mackolil, and S. M. Mallikarjunaiah, Response surface optimization of heat transfer rate in Falkner–Skan flow of ZnO–EG nanoliquid over a moving wedge: Sensitivity analysis, Int. Commun. Heat Mass Transf. **125**, No. 1 (2021) 105348.

[29] K. S. Mekheimer, Effect of the induced magnetic field on peristaltic flow of a couple stress fluid, Phys. Lett. A **372**, No. 23 (2008) 4271–4278.

[30] S. Nadeem and S. Akram, Peristaltic flow of a couple stress fluid under the effect of induced magnetic field in an asymmetric channel, Arch. Appl. Mech. **81**, No. 1 (2011) 97–109.

[31] S. Nadeem, S. Ahmad, and N. Muhammad, Computational study of Falkner–Skan problem for a static and moving wedge, Sens. Actuators B: Chem. **263**, No. 1 (2018) 69–76.

[32] S. Nasir, S. Sirisubtawee, P. Juntharee, A. S. Berrouk, S. Mukhtar, and T. Gul, Heat transport study of ternary hybrid nanofluid flow under magnetic dipole together with nonlinear thermal radiation, Appl. Nanosci. **12**, No. 9 (2022) 2777–2788.

[33] A. Postelnicu, Thermophoresis particle deposition in natural convection over inclined surfaces in porous media, Int. J. Heat Mass Transf. **55**, No. 7–8 (2012) 2087–2094.

[34] M. M. Rahman and A. Postelnicu, Effects of thermophoresis on the forced convective laminar flow of a viscous incompressible fluid over a rotating disk, Mech. Res. Commun. **37**, No. 6 (2010) 598–603.

[35] M. Ramzan, H. Akhter, N. Shahmir, S. Alkarni, Y. Zhang, and S. Kadry, Influence of inclined magnetic field and surface catalyzed reactions on a ternary hybrid nanofluid rotating flow with irreversibility analysis, ZAMM–J. Appl. Math. Mech. **104**, No. 11 (2024) e202400178.

[36] M. Ramzan, M. U. Khan, N. Shahmir, H. Alotaibi, T. Mehmood, S. Kadry, and M. Hussien, Impact of low oscillating magnetic field on ternary hybrid nanofluid flow between two spinning disks with Thompson and Troian slip and modified Fourier's law, Chem. Phys. Lett. **850**, No. 1 (2024) 141456.

[37] M. Ramzan, S. Naseer, N. Shahmir, M. H. Alshehri, C. Liu, and S. Kadry, Thompson and Troian slip effect on ternary nanofluid flow over a stretching surface influenced by induced magnetic field and surface catalyzed reaction, Numer. Heat Transf. Part A: Appl. **85**, No. 19 (2024) 3131–3146.

[38] P. Rana and G. Gupta, Numerical and sensitivity computations of three-dimensional flow and heat transfer of nanoliquid over a wedge using modified Buongiorno model, Comput. Math. Appl. **101**, No. 1 (2021) 51–62.

[39] P. Rana, S. Gupta, I. Pop, and G. Gupta, Three-dimensional heat transfer of 29 nm CuO–H_2O nanoliquid with Joule heating and slip effects over a wedge surface, Int. Commun. Heat Mass Transf. **134**, No. 1 (2022) 106001.

[40] M. M. Rashidi, N. V. Ganesh, A. A. Hakeem, and B. Ganga, Buoyancy effect on MHD flow of nanofluid over a stretching sheet in the presence of thermal radiation, J. Mol. Liq. **198**, No. 1 (2014) 234–238.

[41] S. Rosseland, Astrophysics: On the Basis of Atomic Theory, (1931).

[42] K. Sakkaravarthi, P. B. A. Reddy, and I. Sakthi, Entropy optimization in Casson tetra-hybrid nanofluid flow over a rotating disk with nonlinear thermal radiation: A Levenberg–Marquardt neural network approach, J. Comput. Des. Eng. **11**, No. 5 (2024) 333–354.

[43] S. Z. Shah, H. A. Wahab, A. Ayub, Z. Sabir, A. Haider, and S. L. Shah, Higher order chemical process with heat transport of magnetized cross nanofluid over wedge geometry, Heat Transfer **50**, No. 4 (2021) 3196–3219.

[44] N. Shahmir, M. Ramzan, C. A. Saleel, and S. Kadry, Impact of induced magnetic field on ferromagnetic ternary and hybrid nanofluid flows with surface catalyzed reaction and entropy generation assessment, Numer. Heat Transf. Part A: Appl. **86**, No. 7 (2025) 1839–1859.

[45] S. A. Shehzad, F. M. Abbasi, T. Hayat, and F. Alsaadi, MHD mixed convective peristaltic motion of nanofluid with Joule heating and thermophoresis effects, PLoS One **9**, No. 11 (2014) e111417.

[46] I. Siddique, Y. Khan, M. Nadeem, J. Awrejcewicz, and M. Bilal, Significance of heat transfer for second-grade fuzzy hybrid nanofluid flow over a stretching/shrinking Riga wedge, AIMS Math. **8**, No. 1 (2023) 295–316.

[47] X. Su, L. Zheng, X. Zhang, and J. Zhang, MHD mixed convective heat transfer over a permeable stretching wedge with thermal radiation and ohmic heating, Chem. Eng. Sci. **78**, No. 1 (2012) 1–8.

[48] C. Sulochana, S. R. Aparna, and N. Sandeep, Heat and mass transfer of magnetohydrodynamic Casson fluid flow over a wedge with thermal radiation and chemical reaction, Heat Transfer **50**, No. 4 (2021) 3704–3721.

[49] A. Wahab, M. I. Asjad, K. Anjum, and S. Khan, Computational Modeling of Casson Blood Flow in Symmetrically Stenosed Carotid Arteries Based on Finite Volume Scheme, Punjab Univ. J. Math. **57**, No. 1 (2025) 43–63.

[50] I. Waini, A. Ishak, and I. Pop, MHD flow and heat transfer of a hybrid nanofluid past a permeable stretching/shrinking wedge, Appl. Math. Mech. **41**, No. 3 (2020) 507–520.

[51] J. Wang, Y. Zhai, P. Yao, M. Ma, and H. Wang, Established prediction models of thermal conductivity of hybrid nanofluids based on artificial neural network models in waste heat system, Int. Commun. Heat Mass Transf. **110**, No. 1 (2020) 104444.

[52] F. M. White and J. Majdalani, Viscous Fluid Flow, McGraw Hill, **3** (2006) 433–434.

[53] Y. J. Xu, M. Bilal, Q. Al-Mdallal, M. A. Khan, and T. Muhammad, Gyrotactic micro-organism flow of Maxwell nanofluid between two parallel plates, Sci. Rep. **11**, No. 1 (2021) 15142.

[54] N. A. Zainal, R. Nazar, K. Naganthran, and I. Pop, Flow and heat transfer over a permeable moving wedge in a hybrid nanofluid with activation energy and binary chemical reaction, Int. J. Numer. Methods Heat Fluid Flow **32**, No. 5 (2022) 1686–1705.